GOCAD ENSG Conference
3D Modeling of Natural Objects : A Challenge for the 2000's
4 - 5 June 1998

Importance of 3D modeling in understanding high pressure developments : The Greater Alwyn Area - Viking Graben - North Sea

Dominique Bruel [(1)], Elisabetta Preziosi [(1)] and Philippe Renard [(2)]

[(1)] CIG, Ecole des Mines de Paris, 77305 Fontainebleau, France.
E.mail: bruel@cig.ensmp.fr - Phone: 33 01 64 69 47 54 - Fax: 33 01 64 69 47 03
[(2)] ETH Hoenggerberg, Zurich - Switzerland
E.mail: renard@erdw.ethz.ch - Phone: 41 1 633 68 36 - Fax: 41 1 633 11 08

1 Introduction

The study concerns a ~ 80 km $\times$ 80 km area which is a part of the East Shetland Platform located at the western margin of the Viking Graben. The basin exhibits sandstone/shale alternances and is affected by NNW-SSE trending faults. Neighbouring oil fields, known as Alwyn-North and Dunbar, present different abnormal pressure developments and diagenetic signatures. Overpressures as large as 20 to 35 MPa are found in sandstone reservoirs in the East-southern part of the area. Illitisation is reported [1] which results in drastic changes in the hydraulic properties of some reservoirs (Moss B., [2]).

In this paper, we present some model results from a new three-dimensional basin modeling code (NEWBAS [3]). The first objective of this study is to reconstruct the deposition process and to simulate during time the evolution of past fluid migrations and thermal regimes. Particular attention is given here to overpressure generation linked with the deposition of low permeability facies at spatially highly variable rates. The final purpose remains the identification of a mechanism in open systems that might be responsible for diagenetic effects, and which would exhibit spatial variability at the regional scale.

2 Methods

2.1 Model description

NEWBAS is a three-dimensional, fluid flow, compaction model, which allows for the deposition of sediments at variable rates, and handles erosion phases and unconformities. Lateral extention of the deposits as well as stratigraphic variations are accounted for transiantly, so that the three-dimensional morphology of the sedimentary pile is truly reproduced. Faulted patterns can be considered but some simplifications are necessary. Only vertical displacements

are considered. A differential vertical motion of two adjacent blocks greater than the sum of the half-thickness of each one, results in the presence of a fault, acting as an impervious barrier.

Main principles are summarised in the Annex 1, (tab. 3) and briefly described here after, using the notations and symbols defined in table 1. The mass balance principle is applied for both fluid and solid phases, and the corresponding equations take the form given in (1) and (2). Fluid motion is governed by Darcy's law (3), and the main driving forces derive from pressure gradients combined with buoyency effects. Permeability is dependent on porosity, according to a modified Koseny-Carman relationship, and is anisotropic. Indeed permeability values in any layer may significantly differ from the one perpendicular to it. Porosity is related to the effective stress prevailing at depth (see equations (4) and (6)), as depicted by the non-linear function (5). All the mechanical effects governing compaction are mono-dimensional, and are evaluated along the vertical direction.

H_w	sea-water depth	[m]	ϕ	porosity	[%]
ρ_w	fluid density	$[kgm^{-3}]$	ρ_s	solid density	$[kgm^{-3}]$
λ_w	fluid heat conductivity	$[Wm^{-1}K^{-1}]$	λ_s	solid heat conductivity	$[Wm^{-1}K^{-1}]$
C_w	fluid heat capacity	$[JK^{-1}kg^{-1}]$	C_s	solid heat capacity	$[JK^{-1}kg^{-1}]$
V_w	fluid velocity	$[ms^{-1}]$	V_s	solid velocity	$[ms^{-1}]$
Q_w	source term for fluid	$[s^{-1}]$	Q_s	source term for solid	$[s^{-1}]$
K	permeability	$[m^2]$	μ_w	fluid viscosity	$[Pas]$
P	fluid pressure	$[Pa]$	g	gravity	$[ms^{-2}]$
σ	effective stress	$[Pa]$	S_g	total stress	$[Pa]$
z	depth coordinate	$[m]$	t	time	$[s]$

Table 1: Notations and symbols used in the mathematical formulation.

$$\frac{\partial}{\partial t}(\phi\rho_w) + \mathrm{div}\,(\phi\rho_w \vec{V}_w) = Q_w\,\rho_w \tag{1}$$

$$\frac{\partial}{\partial t}((1-\phi)\rho_s) + \mathrm{div}\,((1-\phi)\rho_s \vec{V}_s) = Q_s\,\rho_s \tag{2}$$

$$\vec{U} = \phi\,(\vec{V}_w - \vec{V}_s) = -\frac{\bar{\bar{K}}}{\mu_w}\,(\overrightarrow{\mathrm{grad}}\,P - \rho_w g\,\overrightarrow{\mathrm{grad}}\,z) \tag{3}$$

$$\sigma(\phi) = Sg - P \tag{4}$$

$$\phi(\sigma) = \phi_r + \phi_1 \exp(\frac{-\sigma}{\sigma_1}) + \phi_2 \exp(\frac{-\sigma}{\sigma_2}) \tag{5}$$

$$S_g = g \int_0^z (\rho_w \phi + \rho_s (1-\phi))\, du + g \int_0^{Hw} \rho_w \, du \tag{6}$$

Rewritting the second-order diffusivity equation and discretising it in a finite-volume approach, for a multi-layered orthogonal mesh (nested-square pattern) leads to the formulation (7), in which S_{li} are the contact surfaces of cell l with neighbouring cells i and Ω_l is the volume of the current cell l.

$$\sum_{i \neq l} S_{li} k_{li}^{n+1} [\frac{P_l^{n+1} - P_i^{n+1}}{\Delta x_{li}}] \Delta t =$$
$$\sum_{i \neq l} S_{li} k_{li}^{n+1} \rho_i g [\frac{z_l^{n+1} - z_i^{n+1}}{\Delta x_{li}}] \Delta t + [\frac{\phi_l^n}{1-\phi_l^n}] \rho_w \Omega_l^n - [\frac{\phi_l^{n+1}}{1-\phi_l^{n+1}}] \rho_w \Omega_l^{n+1} + Q_{wl} \tag{7}$$

Linearization of $\frac{\phi_l^{n+1}}{1-\phi_l^{n+1}}$ at time $n+1$ and iteration k is given by $\frac{\phi_l^{k+1}}{1-\phi_l^{k+1}} = \frac{\phi_l^k}{1-\phi_l^k} + \frac{\delta\phi_l^k}{(1-\phi_l^k)^2}$ with $\delta\phi_l^k = 1/(\frac{\partial\sigma}{\partial\phi})_l^k \times [-\delta P_l^k + Sg_l^k - P_l^k - \sigma_l(\phi_l^k)]$

and $(\frac{\partial\sigma}{\partial\phi})_l^k$ derived explicitly from (5) in the general case of compaction. For erosion accompanied by a decrease of the effective stress level, an elastic rebound may be introduced.

The set of equations 7 is solved for pressure using a combined Picard-Newton iterative scheme. Convergence is checked after each iteration, according to a prescribed pressure closure criterion. Secondary unknowns, such as porosity, depth or fluid velocities, are then obtained. Over pressure are derived by simple difference in between the calculated pressure and the static pressure level.

Because the thermal problem is of major concern for related diagenetic studies in this area, a similar numerical algorithms was developed to solve for the 3D temperature distribution T across the basin, assuming conduction and convection are the major governing processes (see eq. (8) below).

$$\frac{\partial \rho_{av} C_{av} T}{\partial t} = div\ (\lambda\ grad\ T) - div(\rho C V_s T) - div(\rho_w C_w \phi (V_s - V_w) T) + q_r \tag{8}$$

In these calculations, radiogenic volumetric source term q_r might be considered. Following the above notations, we define equivalent sediment properties as follows :

$\rho_{av} C_{av} = \phi \rho_w C_w + (1-\phi) \rho_s C_s$ and $\lambda = \lambda_w^{\phi} \lambda_s^{(1-\phi)}$

Heat flux is prescribed at the interface with the basement, and can be variable in space and time. At the top of the sedimentary pile, sea water or air temperature are prescribed.

In turn, temperature is used to update fluid density and fluid viscosity in the fluid flow compaction problem at each time step.

2.2 Data requirements

Reconstructing the basin history requires two types of data. The first set incorporates a current description of the sedimentary object in a 3D space, and the times of geological events, geologic stages, as well as stratigraphy and paleobathymetry. At this stage, seismic data combined to borehole observations are of the most valuable source of information to establish the present day maps of sediment thicknesses.

The second set of data concerns the physical properties of the various type of deposits identified during the successive sedimentary intervals. Mostly porosity-depth curves depicting the behavior of the various lithological composition have to be collected. These are used in a standard backstripping process to evaluate past sedimentation rates. Other lithology-specific parameters are also required, to evaluate effective stresses and determine permeabilities or thermal properties during the direct basin modeling.

3 Building the 3D model of the Greater-Alwyn area

3.1 Geological setting

The 80 km^2 area of the model is located in the East Shetland Platform, in the northern North Sea. The geological frame of the Alwyn area was described by [6] and [7].

During the Permo-Triassic period a tensional regime in the region generated a major fault pattern N-S and secondary faulting in ENE-WSW transverse direction. Faults were active during Jurassic, producing variable thickness of the syn-tectonic formations throughout the area. The N-S fault system gave rise to the westward dipping rotated fault blocks, which now constitute structural traps.

By the end of the Jurassic, major tectonic activity had ceased in the Alwyn area and during the Cretaceous-Tertiary a thick marine essentially shaley sequence covers the extensional structures and seals the Jurassic faults, in a post-rift thermal subsidence regime.

During the Triassic perriod, continental sedimentation occurred, producing the red-bed deposits of the Cormorant Formation (not considered in the model). The Jurassic includes 4 major groups :

- The Statfjord Fm. (Rhaetic-Lias). Essentialy sandy fluvio-deltaic sequences, passing to marine sedimentation during the Sinemurian.
- The Dunlin Gp. (Lias). Prevailing shaly, marine.

- The Brent Gp. (Dogger). Main reservoir in the area, corresponds to a northward prograding delta. A short period of continental more argillaceous sedimentation interrupted the prevailing sandy marine sequence.
- The Humber Gp. (Callovian-Kimmeridgian). Composed by two syn-tectonic shaley formations: the Heather Fm. (Bathonian-Oxfordian) and the euxinic Kimmeridge Clay Fm. (late Oxfordian - late Ryazanian); due to the syn-tectonic deposition, their thickness is strongly variable. The Kimmeridge Clay Fm. is the main source-rock in the region (average TOC 5%).

The regional Cimmerian unconformity (Rawson & Riley, 1982) bounds the Jurassic sedimentation. The Cretaceous includes two groups :

- The Cromer Knoll Gp. (Lower Cretaceous), prevailing shaley but including some marls and limestones.
- The Shetland Gp. (Upper Cretaceous), composed mainly by marls and shales, whose thickness varies from 0 to 2000 m in the study area.

The Tertiary is a thick silty-shaley sequence, much more uniform in thickness. For the model purpose it was divided in three intervals :

- Palaeocene, silty.
- Eocene, more shaley.
- Oligocene-present day, again silty.

3.2 Assembling the 3D numerical model

3.2.1 Selected time intervals

Every time interval translates into a numerical layer in the NEWBAS approach. Thus we can distinguish deposition events, non deposition events or erosional events (although no erosional events are considered in this model).

The Triassic-Present day sequence was divided into 9 stratigraphic intervals, from Upper Triassic to present day. For each one, geometry and lithological contents were inferred from well stratigraphy and seismic maps [8] . In addition, the time span corresponding to the late Jurassic-Early Cretaceous hiatus is represented by a numerical layer. Due to their thickness, the Oligocene-Present day interval and the Upper Cretaceous were divided into 3 intervals each, thus the final number of model layers adds up to 14.

3.2.2 Thicknesses

The extent of Jurassic and Cretaceous formations is not continuous over the model area, major gaps existing in the SW edge. They were all interpreted as several local hiatus. A major hiatus corresponds to the Cimmerian unconformity; its time span was determined on the basis of the stratigraphic gaps observed at several wells in the area. In spite of the variability of the time duration of this discontinuity (up to a maximum hiatus from Kimmeridgian to Cenomanian), a uniform sedimentation interruption from 150 million years to 119 milllion years (Kimmeridgian-Barremian) was considered.

The 3D geometry of the model area was reconstructed on the basis of the two-way-times seismic maps of the reflectors corresponding to the nine choosen isochrone surfaces. A modified 'layer cake' method was used for the time to depth conversion, using a 110 borehole dataset to fit the velocity models.

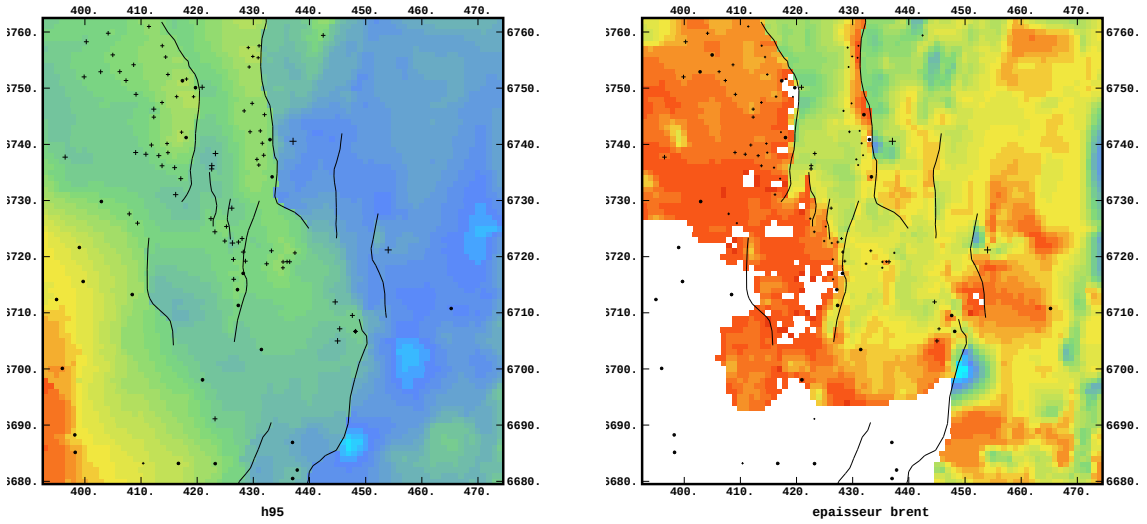

Figure 1: Brent formation: crosses refer to the borehole locations and lines reflect the local but simplified faulted pattern affecting the Brent formation. (left) Top of the brent after time-depth conversion, (right) Thickness, ranging from 0 m (red) to 500 m (blue).

3.2.3 Facies generation

Lithological maps for each interval were generated using geostatistics, based on of the lithological information from a number of wells (24 in the lower to 36 in the upper intervals). A simplified preliminary model was made, in which lithological class was given to each node and only three classes were considered. As a result, lithological variation within each layer is very poor, and limited to the field areas.

The procedure used is the following. Firstly, for each stratigraphic interval a simplified

lithological composition was given to nodes corresponding to boreholes, using a 4 end-members scheme, specifying the proportion of sandstone, siltstone, clay and limestone for that node. Secondly, co-kriging of estimated proportions was performed, to calculate the variation maps of the selected lithologies. Finally, the continuously varying proportions of the 4 components was transformed in a simple class distribution map for each layer, where 3 classes were considered: 'sand', corresponding to a lithological composition with less than 33% of clay, 'silt', with clay varying form 33 to 66%, 'clay', with more than 66% of clay.

Limestone, scarcely present as a whole, but representing an average of 20% in the Lower Cretaceous, was at this stage, treated as equivalent to sand. Similarly, at this stage, silt was treated as equivalent to a composition of 50% sand and 50% clay.

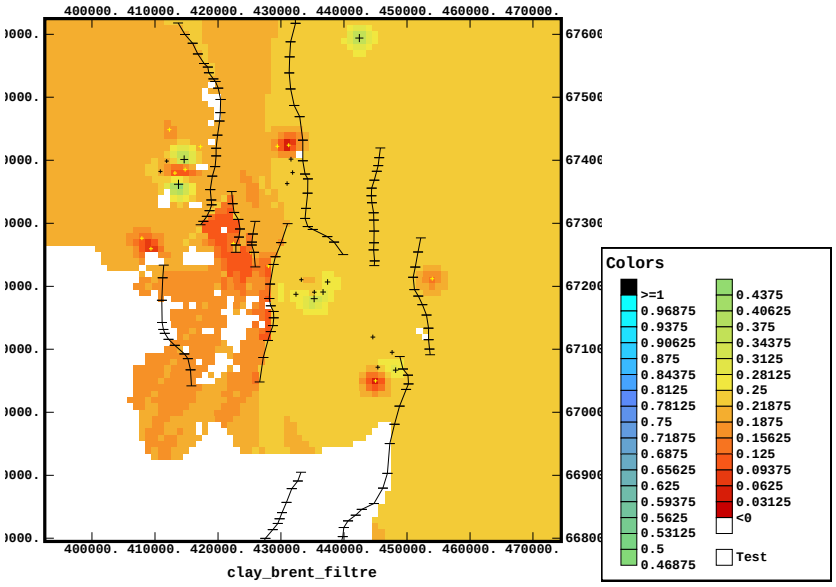

Figure 2: Map of kriged proportion of the clay facies in the brent layer. Note the extension of the brent, the trace of the fault and the bore-holes where facies inputs were available.

3.2.4 Other main parameters

Paleobathymetry is prescribed at the different dates, according to the scenario depicted in [5]. The current water depth is fixed at 150 m. A maximum of 300 m is applied during tertiary, while no water is assumed during the Cimmerian unconformity. Low water depths in the order of 50 m are used during the Jurassic. Heat fluxes are between 0.042 Wm^2 and 0.051 Wm^{-2} as stated by the same authors [5].

4 Pressure modelling

4.1 First results

Because the aim of the modeling is not a real calibration of a large number of parameters against pressure maps at different dates, we do not follow a complete optimisation process. Instead we look for some tractable procedure to bracket the calculated pressures at particular boreholes where measurements were made available, for instance at the Hild reservoir, (well 30 7-8), and and so derive some regional pressure trends. Values as large as 35 MPa are known in the Brent formation at the Hild reservoir, 21 MPa at Alwyn-South and 15 MPa at the Alwyn-North and Ninian Brent reservoirs [4].

Our initial calibration approach involves a previous set of 2D calculations, performed on a series of East-West vertical cross-sections extracted from the 3D model. An example is given in figures 3 and 4, which corresponds to a section at coordinate y=6707 km in figure 1.

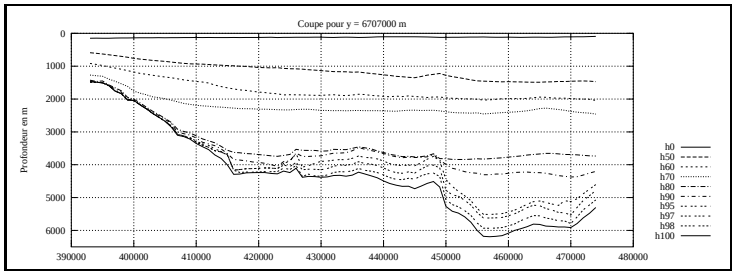

Figure 3: Basin geometry along the cross-section 6707.

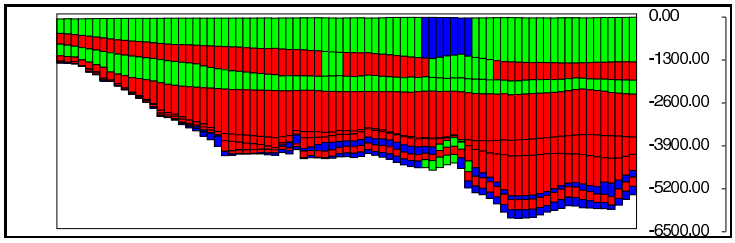

Figure 4: Cross section 6707. Lithology after simplification into a three class system. Sandy (blue), silty (green) facies, shaley (red) facies.

For each lithology, petrophysical parameters were obtained from literature, in particular the porosity-depth curves. Some sensitivity analysis was performed for the specific surface of 'clay' because it was thought that this was the key free parameter factor for the overpressure modelling, since sedimentation rates were prescribed by the geometry. Permeabilities are therefore in the range of 10^{-12} to 10^{-20} m^2.

These calculations involved a limited number of unknowns (no more than 80×14 cells per section opposed to the 2600×14 cells required in the global 3D description) and therefore were very fast. Typical time steps of 0.1 MY were found sufficient for numerical convergence.

Lithology	ϕ_0 %	ϕ_r %	k_v/k_h	S_0 m^2/m^3	λ_s $W/m{\cdot}K$	C_s $J/kg{\cdot}K$	ρ_s kg/m^3
Sand	0.49	0.026	1.	9.010^5	2.8	1080.	2650.
Silt	0.56	0.022	0.5	3.010^7	2.5	950.	2680.
Shale	0.63	0.028	0.4	5.010^8	2.0	840.	2720.

Table 2: Parameters used in the first calibration attempt. ϕ_0 is the initial porosity at the date of deposition and ϕ_r is the residual porosity.

This first set of results, shown in figure 5, refers to the 2D model of cross-section 6707. Geometry, porosity, pressure, over-pressure and temperature distributions are displayed at the present day in the left part of the diagram. A maximum of 25 MPa is predicted in the Dunlin group which roughly agrees with in situ observations. However pressures are nearly uniform in the deep western part of the modeled area, as a consequence of the fault pattern at km 445 which prevents the trapped fluid from escaping to the west.

The same set of parameters was then used as a starting point for 3D modelling. 3D results concerning abnormal pressures are compared to the previous 2D analysis. Interestingly, similar permeability distributions lead to lower overpressure levels in the Brent, by a factor two (see right hand side in figure 5 and figure 6). The maximum is now located in the thick Jurassic shaley layer (Humber Gp.), and lower values are simulated in the underlying Brent reservoir.

4.2 Discussion

The discrepency between results from 2D calculations, and 2D results extracted from 3D calculations is clearly due to the three-dimensional nature of the flow pattern through the heterogeneous rock masses. It reflects here a South to North component to the flow that can not be represented by cross section models, perpendicular to the main axis of the graben.

As a consequence, any attempt to interpolate between a series of parallel 2D sections to reconstruct an equivalent 3D volume is likely to produce large errors in physical parameter estimates for this particular case.

New estimates for the parameters are required to better match the observed overpressure profiles and we focussed on the clay permeability parameters, keeping everything else constant. A significant improvement was gained by decreasing the clay permeability by nearly one order of magnitude. This can be done by using an increased anisotropy factor k_v/k_h equal to 0.1. Alternativaly larger specific area parameters, S_0, can be used, with suitable values lying in the range $8.10^8 - 10^9\ m^2/m^3$ instead of $5.10^8 m^2/m^3$. This is illustrated in figure 8.

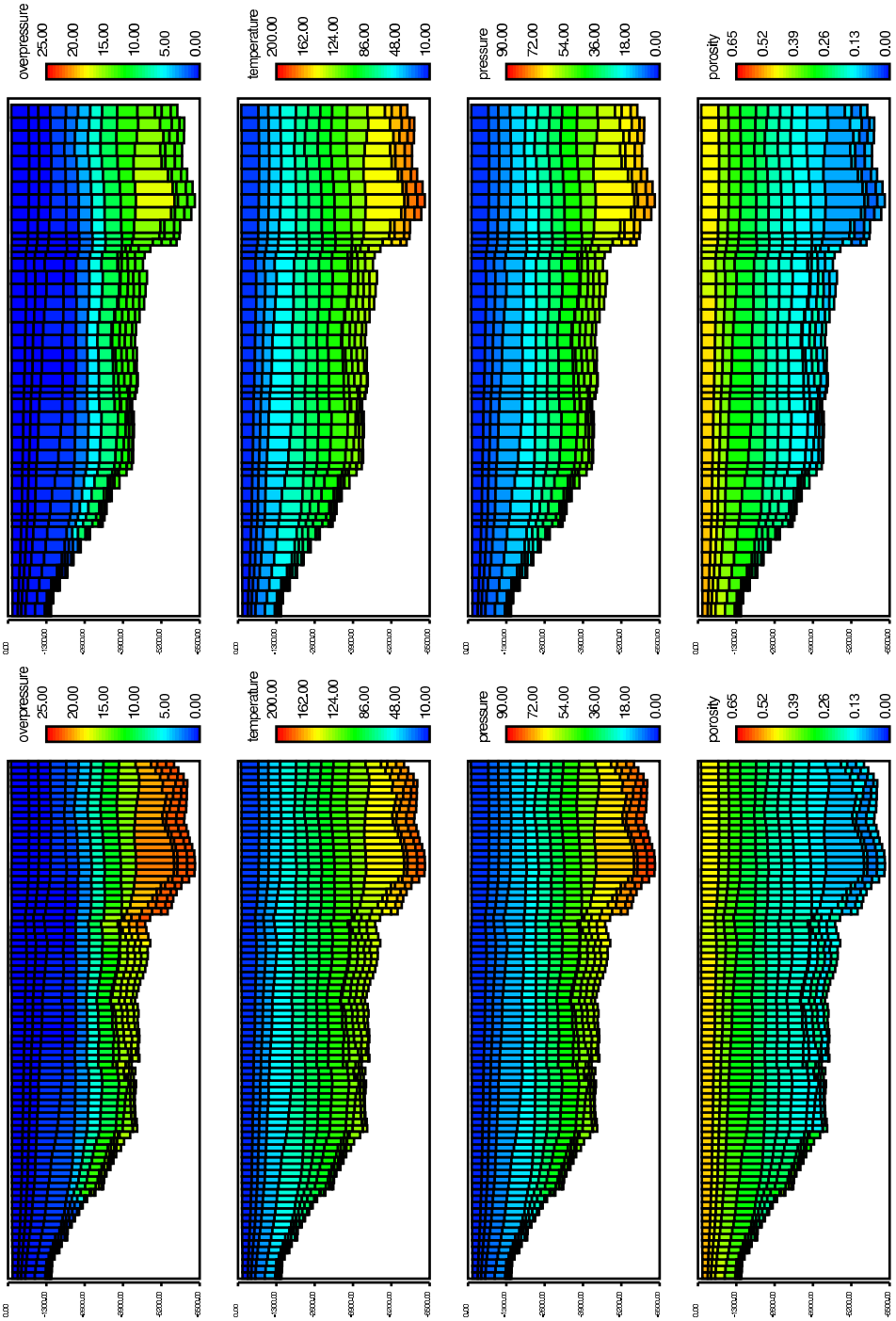

Figure 5: Present day overpressure [MPa], temperature [°C], pressure [MPa] and porosity distributions, in two dimensions calculations (left hand side), along the 6707 section. On the right, corresponding distributions extracted from the 3D calculations along the same section. Note the 1 km cell-size in the 2D approach and the mixed 1 km - 2 km cells in the 3D approach.

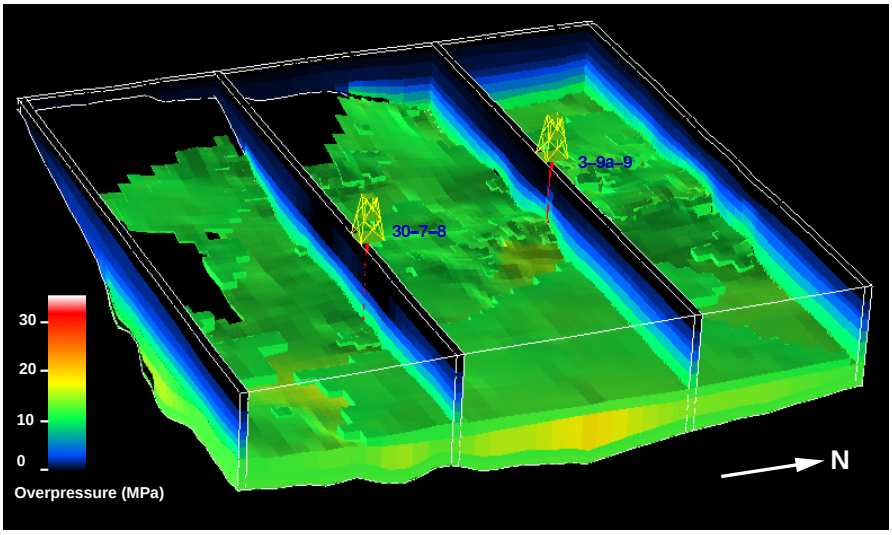

Figure 6: Areas where overpressures are larger than 11 MPa. Reference set of parameters derived from the previous 2D analysis.

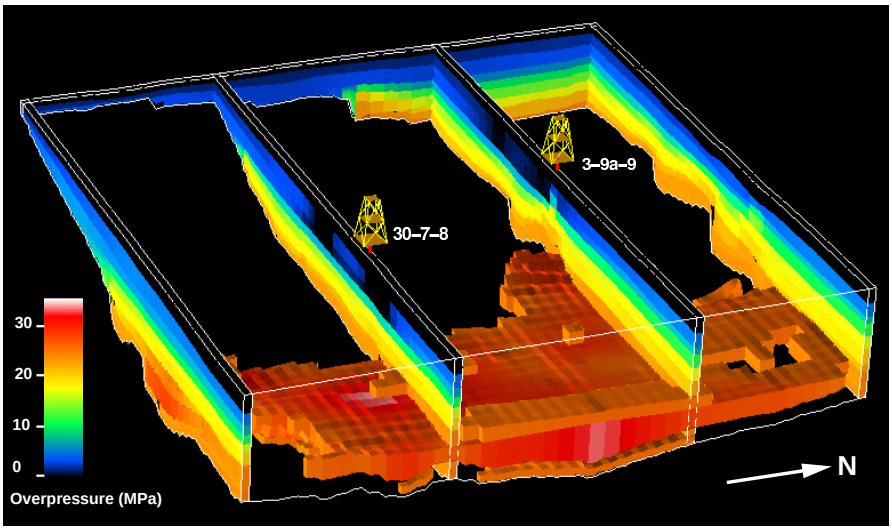

Figure 7: Areas where overpressures are larger than 25 MPa. Updated set of parameters.

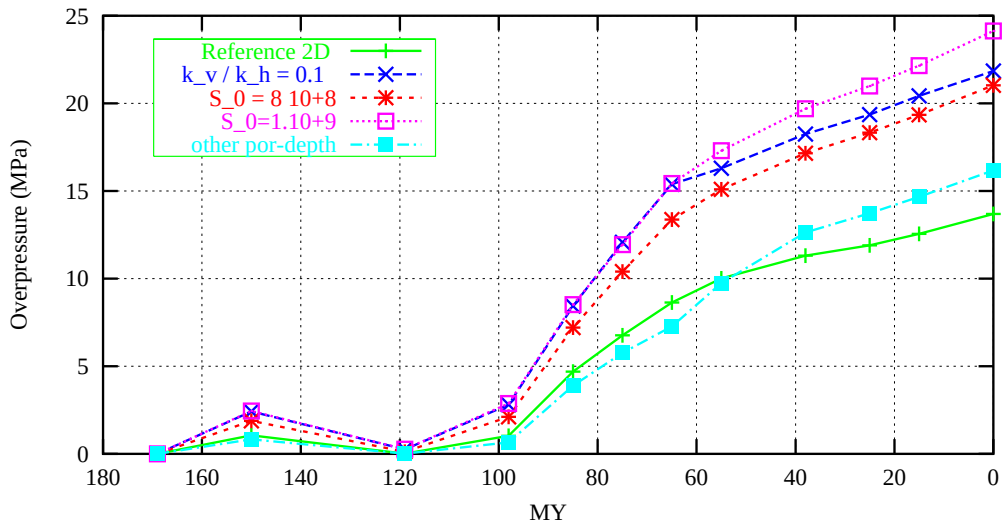

Figure 8: Brent: Evolution of overpressures at km 445 (Well 30 7-8, Hild reservoir, in section 6707), resulting from 3D calculations. X axis refers to time before present.

The 3D graphic built for the case with $S_0 = 10^9 m^2 m^{-3}$, figure 7, shows the areas where overpressures are in excess of 25 MPa. These are clearly located in the deep shale dominated section (late Jurassic, eastern part of the modelled area). It shows that fluid can escape through the Brent formation. However the pressure global trend [4] is not really reproduced as a probable consequence of too uniform a description of the lythologies. Further work in this area is in progress and will be based on a system of five classes for the lithology description.

Acknowledgements

The work reported here forms part of the GDR TRABAS (CNRS) research programe, with financial support of TOTAL, ELF, IFP and ANDRA. We are grateful to TOTAL Norge for providing data from the NOPEC northsea digital atlas. Special thanks to J.C. Lacharpagne, C.Sejourne and F. Sommer for helpful discussions and to C. de Fouquet for helping us in using the ISATIS package for geostatistics.

5 References

[1] GDR CNRS TRABAS. "Transfert dans les bassins sédimentaires", *LGA- Université Paris VI, IFP-EAP-TOTAL-ANDRA, rapport final, mars 1998*

[2] Moss B. "The petrophysical characteristics of the Brent sandstones". *Geology of teh Brent Group*, Morton et al. eds, *Geol. Soc. Sp. publ.* 61, 471-496, 1992.

[3] Belmouhoub R. "Modélisation tridimensionnelle Hydro-Thermo-Mécanique d'un bassin au cours de son histoire géolgique." *Thèse de l'Ecole des Mines de Paris*, 1996.

[4] Buhrig C.. Geopressured jurassic reservoirs in the Vikinng graben: modelling and geological significance. Marine and Petroleum Geology, 6, 31-48, 1989.

[5] Dahl, B. E. Nysaether, G. Speers et A. Yukler. Oseberg aerea integrated basin modelling. In J. Brooks et K. Glennie (Eds), Petroleum Geology of North West Europe, pp.1029-1037, Graham and Trotman, 1987.

[6] Johnson, A. et M. Eyssautier. Alwyn north field and its regional context. In J. Brooks and K.W. Glennie (Eds), Petroleum Geology of North West Europe, pp. 963-977. Graham and Trotman. 1987.

[7] Inglis, I. and J. Gerard. Alwyn north field. In I.L. Abbotts Ed., United Kingdom Oil and Gas Fields 25 years commemorative volume, pp21-32. The Geological Society, 1991.

[8] North Sea Digital Atlas. NOPEC.

Annex 1: Principles of the numerical model

	NEWBAS: Heat and solute transfer during geologic time in heterogeneous sedimentary basins	parameters
Geometry	3D, evolutive, derived from a backstripping analysis *deposition phases* *non deposition phases* *erosion sequences*	$\varphi_{observed}(X,t)$
Hydraulic	mass conservation equations Darcy's law - single phase porosity-permeability Koseny-Carman's relation $K(\varphi) = \frac{0.2\varphi^3}{S_0^2(1-\varphi)^2}$ anisotropy $[K]=K(\varphi)\begin{bmatrix}\lambda_s & 0 & 0\\ 0 & \lambda_s & 0\\ 0 & 0 & \lambda_z\end{bmatrix}$ fluid viscosity μ_w and density ρ_w as functiun of temperature θ	 S_{0i} $(\lambda_s,\lambda_z)_i$
Mechanic	solid mass conservation vertical deformation Terzaghi effective stress principle $\sigma = S_V - \psi$ empiric relationship $\varphi = \varphi_r + \varphi_1 exp(-\sigma/\sigma_1) + \varphi_2 exp(-\sigma/\sigma_2)$ compaction remains quasi-irreversible elastic rebound may be allowed if σ decreases	 $(\rho_s)_i$ $(\varphi_r,\varphi_1,\sigma_1,\varphi_2,\sigma_2)_i$ E_i
Thermic	heat conservation (conduction + convection) radiogenic volumic heat source	$(\lambda_{th},\gamma_{th})_i$ r_i
Boundaries	top: prescribed pressure + temperature (*paleobathymetry + eustatism*) lateral: hydrostatic or no flow bottom: free for mechanic, impervious basement, basal heat flux	 $\Phi(X,t)$
Numerics	finite volumes method discretisation using nested square meshes principal unknown : field pressure ψ iterative Newton + Picard processes for non-linearities $\varphi(\sigma)$	
Results	pressure fied $\psi(X,t)$, porosity distribution $\varphi(X,t)$ temperature field $\theta(X,t)$, overpressures, fluid velocities	

Table 3: Model description. Subscript i refers to the type of lithology. X and t denote space and time respectively.

Annex 2: Heat flux and Paleobathymetry

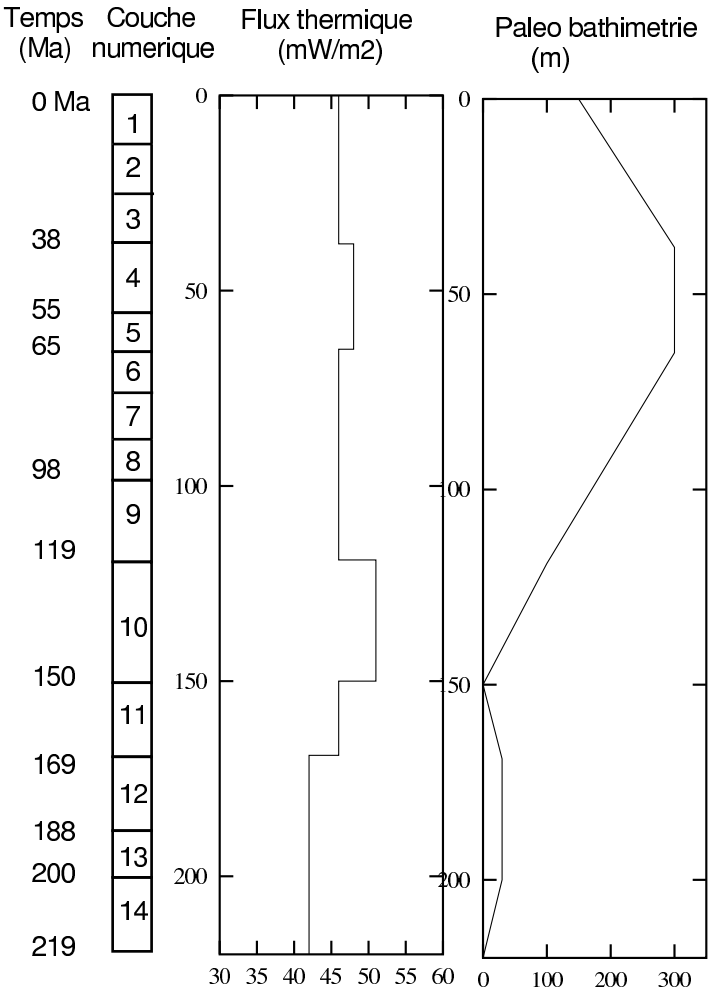

Figure 9: Paleobathymetry and heat flux at the basement interface selected to perform the numerical simulations

Annex 3: History of the Alwyn basin

Surface (nbgeo)	Couche numérique	Age (Ma) Phase	Bathim. (m)	Flux therm.
1		0	Actuelle	
	1: Oligocène - Actuel	Dépôt		0,046
2		38	300	
	2: Eocène	Dépôt		0,048
3		55	300	
	3: Palocène	Dépôt		0,046
4		65	300	
	4: Shetland Gp.	Dépôt		0,046
5		98	100	
	5: Cromer Knoll Gp.	Dépôt		0,046
6		119	100	
	6: Lacune cimmérienne	Non-dépôt		0,051
7		150	0	
	7:Humber Gp.	Dépôt		0,046
8		169	30	
	8:Brent Gp.	Dépôt		0,042
9		188	30	
	9:Dunlin Gp.	Dépôt		0,042
10		200	30	
	10:Statfjord Gp.	Dépôt		0,042
11		219	0	

Table 4: Schematisation de la subdivision de l'histoire sédimentaire en couches numériques.